CHEMISTRY OF MATERIALS

pubs.acs.org/cm

Article

Thermally Induced Structural Reordering in Li- and Mn-Rich Layered Oxide Li Ion Cathode Materials

Florian Sigel, Björn Schwarz, Karin Kleiner, Christoph Dräger, Lars Esmezjan, Murat Yavuz, Sylvio Indris,* and Helmut Ehrenberg

Cite This: *Chem. Mater.* 2020, 32, 1210−1223

Read Online

ACCESS | Metrics & More | Article Recommendations | Supporting Information

ABSTRACT: In recent years, a considerable amount of effort has been put into a better understanding of the correlation of structure and electrochemical properties in Li- and Mn-rich NCM layered oxide Li ion battery cathode materials, such as the intensely investigated $Li_{1.2}Ni_{0.15}Co_{0.1}Mn_{0.55}O_2$ composition. A gradual transformation from a trigonal $R\bar{3}m$ layered structure toward a cubic $Fd\bar{3}m$ spinel structure during electrochemical cycling results in an unwanted decay of the mean charge and discharge voltages, called "voltage fade". This transformation proceeds via an interim phase, which is characterized by the local deordering of cations and the introduction of various lattice defects after the formation of the initially well-ordered material. In this study, these structural changes are studied in detail on a long-range atomic scale by synchrotron radiation powder diffraction as well as on a very local atomic scale by ^{7}Li nuclear magnetic resonance and X-ray absorption spectroscopy. A structural reordering was induced by a mild thermal treatment (150−300 °C) in lithiated (discharged to 2.0 V) as well as in delithiated (charged to 4.7 V) electrodes, which results either in a partial recovery of the initial well-ordered state or in an intensification of the structural degradation toward a spinel-type cation ordering, respectively. The structural reordering thus obtained was again studied on a long-range and local atomic scale and correlated with the electrochemical properties. To complement the experiment, an electrochemically highly fatigued electrode (300 cycles, discharged to 2.0 V) showing a pronounced voltage fade was thermally treated, which resulted again in a partial recovery of the initial well-ordered structure and its accompanying electrochemical properties. Finally, the results are summarized in a model explaining the influence of the local cation ordering, lattice defects, and the oxygen sublattice on the electrochemical properties, such as the oxygen redox activity and the voltage fade.

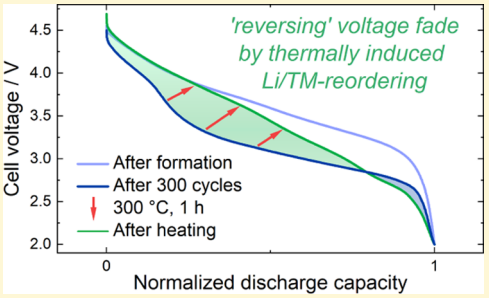

1. INTRODUCTION

Layered transition-metal oxides such as the "Li- and Mn-rich" layered oxides are promising candidates for next-generation Li ion battery cathodes that offer high reversible capacities (>250 mAh/g) and higher safety together with reduced costs.[1] As still under debate, these oxides can be considered as either solid solutions or composites formed between the end members Li_2MnO_3 and $LiTMO_2$ (TM = Ni, Co, Mn) (NCM) or even as a kind of mixture in between these models. For an economic and efficient operation as cathode materials in electrified vehicles for example, knowledge about mechanisms of degradation is mandatory to optimize these materials for longer lifetimes. So far, a gradual decrease of the mean charge and discharge voltage during electrochemical cycling, called "voltage fade", and a pronounced "hysteresis" between charge/discharge are major drawbacks of this material class. Especially, the gradual decrease of the mean voltage is challenging to handle, e.g., by the battery management system and the power control of an electric vehicle. Furthermore, the hysteresis decreases the energy efficiency of the battery. A gradual local cation rearrangement according to a cubic $LiTM_2O_4$-type spinel during de-/lithiation, with a partial reversible character (hysteresis) and a partial irreversible character (voltage fade), is supposed to cause these inefficiencies.[2]

Conventional layered $LiTMO_2$ cathode materials are based on a trigonal α-$NaFeO_2$-type layered structure, which belongs to the space group $R\bar{3}m$. The layered structure is realized by the alternating occupation of octahedral sites in a slightly distorted cubic close-packed oxygen sublattice by lithium (3*b* crystallographic site) and transition-metal ions (3*a* crystallographic site) along the hexagonal *c*-axis in an ABC stacking sequence (O3-type). The formal addition of Li_2MnO_3, which can be rewritten as $Li[Li_{1/3}Mn_{2/3}]O_2$, leads to the partial substitution of TM ions with Li ions in the transition-metal layers. This substitution is realized in an ordered manner, where the Li and TM ions are forming a "honeycomb" ordering scheme within the TM layers (*a*,*b*-plane). The stacking of these layers along the hexagonal *c*-axis leads to a

Received: October 24, 2019
Revised: January 8, 2020
Published: January 8, 2020

https://dx.doi.org/10.1021/acs.chemmater.9b04355
Chem. Mater. 2020, 32, 1210−1223

reduced crystal symmetry and the appearance of additional monoclinic $C2/m$ superstructure reflections in the X-ray diffraction (XRD) pattern. Whereas in pure Li_2MnO_3, all centers of the TM_6 honeycombs are occupied by Li ions, these sites are only partially occupied by Li ions in the studied $Li_{1.2}Ni_{0.15}Co_{0.1}Mn_{0.55}O_2$ material, which is formally composed of 0.5 Li_2MnO_3·0.5 $LiNi_{3/8}Co_{2/8}Mn_{3/8}O_2$. This partial substitution leads to a mixed (Li/TM)-TM_6-type honeycomb ordering within the TM layers.

Unlike the $LiTMO_2$ cathode materials, the Li-rich descendant reveals a pronounced formation process in the initial charge, which is represented by a long "plateau" at around 4.5 V in the electrochemical data. This formation process, often termed "activation", leads to an irreversible structural rearrangement, including the loss of the distinct honeycomb cation ordering,[3] and goes along with the depletion of electrochemically available lithium sites[4] as well as the partial loss of oxygen primarily in the surface layer.[5−7] Moreover, this initial formation process provokes a highly defective structure, which is the onset for the gradual transformation toward a spinel-type cation arrangement.

Several studies showed the importance of structural defects on the electrochemical properties, either for charge balance, e.g., the oxidation of the oxygen lattice[8] and the formation of peroxide species,[9] or presumably inducing voltage/capacity fade and hysteresis such as TMs on tetrahedral interstitial sites,[10−12] Li/TM dumbbells,[11,13] oxygen vacancies,[14] Li^+/H^+ exchange,[15] nanotwins,[16−18] and dislocations.[19] However, due to the high structural complexity of the Li-rich materials, a clear assignment of these structural defects to arising electrochemical features is a rather challenging task.

The motivation of this work is to get more insight into the influence of cation ordering and lattice defects on the electrochemical properties. For this purpose, an initially highly ordered Li- and Mn-rich NCM with nominal composition $Li_{1.2}Ni_{0.15}Co_{0.1}Mn_{0.55}O_2$ was transferred into a highly defective state by electrochemical formation and exposed to a moderate thermal treatment (300 °C, 1 h) to induce a structural reordering toward the thermodynamic equilibrium. The study was carried out for lithiated (discharged to 2.0 V) and delithiated samples (charged to 4.7 V) after the initial formation process as well as for an electrochemically fatigued sample after 300 cycles (2.0 V, lithiated). The therewith-induced structural changes were investigated on the long-range scale by synchrotron radiation powder diffraction (SRPD) as well as on a very local scale by ^{7}Li nuclear magnetic resonance (NMR) and X-ray absorption spectroscopy (XAS) measurements. The detected structural features are correlated with the evolution of the electrochemical characteristics and described in a model providing further insights into the mechanisms involved in the initial formation and the subsequent degradation processes.

2. EXPERIMENTAL SECTION

2.1. Electrode Preparation, Electrochemical Characterization, and Heat Treatment. For the preparation of the cathode electrode sheets, an *N*-methyl-2-pyrrolidone-based slurry of 87% (w/w) $Li_{1.2}Ni_{0.15}Co_{0.1}Mn_{0.55}O_2$ (commercially available HE5050, TODA America), 7% (w/w) poly(vinylidene fluoride), and 6% (w/w) carbon black was die-coated on an aluminum foil (approx. 5 mg/cm^2 active material), dried overnight at 80 °C, and calendered to a final coating thickness of about 30 μm. The electrochemical characterization was carried out in CR2032 coin cells, assembled in an argon-filled glovebox using 12 mm-diameter cathode electrode sheets, two layers of Celgard 2325 as the separator, lithium foil as the anode, and 150 μL of LP30 electrolyte [1 M $LiPF_6$ in 1:1 (w/w) ethylene carbonate (EC)/dimethyl carbonate (DMC)].

The cells were first cycled two times between 4.1 and 2.0 V (wetting cycles), then two times between 4.7 and 2.0 V (formation + after formation cycle), and finally adjusted to 2.0 V (discharged/lithiated sample) or 4.7 V (charged/delithiated sample). All tests were carried out with a current rate of C/10 (1C = 290 mAh/g) at 25 °C with a VMP3 potentiostat (BioLogic). To reduce the duration for the preparation of the highly fatigued sample (300 cycles), the current rate was increased to C/5 after the first 4 cycles (2× wetting, formation, after formation). The last two cycles were carried out in a fresh cell with a new electrolyte and a Li metal counter electrode and a slower current rate of C/10 to identify the degradation features, which can be assigned to the cathode material exclusively.

The cycled electrodes were carefully extracted from the cell stack and washed two times with dimethyl carbonate (DMC) followed by drying under vacuum to remove electrolyte residues. For the heat treatment, the electrodes were placed in a sealable glass tube and transferred from the glovebox into a preheated tubular oven at 150, 200, 250, or 300 °C, sequentially. A maximum value of 300 °C was chosen to prevent the decomposition of electrode additives [binder/carbon, cf. thermogravimetric analysis (TGA) analysis in Figure S1 in the Supporting Information]. After 1 h, the glass tube was removed from the oven and cooled down in the surrounding air without further temperature regulation. Finally, the electrodes were once more assembled, as received after heating, into coin cells with a fresh lithium metal anode and an electrolyte. The electrochemical characterization was carried out within five "post-thermal" cycles and discharged to 2.0 V at the end of the last cycle ("relithiated").

The samples used for the NMR and SRPD investigations were prepared by mechanically removing the electrode powder from the aluminum substrate and transferring the powder into the NMR rotors and XRD glass capillaries. For the hard XAS measurements, the electrodes were glued onto a Kapton tape inside the glovebox, the aluminum substrate was pulled off, and a second Kapton tape was put on top.

2.2. Synchrotron Radiation Powder Diffraction. Ex situ synchrotron radiation powder diffraction experiments were performed in 0.5 mm glass capillaries at the high-resolution beamline P02.1[20] at PETRA III, DESY (Germany), at about 60 keV (λ = 0.2072 Å). A two-dimensional (2D) flat panel detector (PerkinElmer amorphous silicon detector) with an exposure time of 60 s was used for obtaining the diffraction images. Fit2D[21] and FullProf[22] were used for data conversion and Rietveld refinements, respectively.

2.3. Solid-State Nuclear Magnetic Resonance Spectroscopy. For ^{7}Li magic-angle spinning (MAS) NMR, a Bruker Avance 200 MHz spectrometer (4.7 T) with 1.3 mm zirconia rotors and a spinning frequency of 67 kHz was used. The experiments were performed with a rotor synchronized Hahn-echo pulse sequence ($\pi/2-\tau-\pi-\tau$-acquisition), a $\pi/2$ pulse length of 0.6 μs, and a recycle delay of 0.2 s at a frequency of 77.82 MHz. All spectra were acquired at room temperature without further cooling of the probe. An aqueous 1 M LiCl solution was used as the reference for the chemical shift of ^{7}Li (0 ppm). All spectra were normalized according to the number of scans and the sample mass.

2.4. Hard X-ray Absorption Spectroscopy. Hard X-ray absorption spectroscopy (XAS) experiments were carried out at the applied X-ray absorption spectroscopy beamline P65 at PETRA III, DESY.[23] The spectra of Ni, Co, and Mn K edges were recorded in the transmission mode, and the reference spectrum for energy correction was simultaneously collected using the corresponding transition-metal foil.

3. RESULTS

3.1. Thermal Treatment of Discharged Samples (2.0 V). In this section, the results from the thermal treatment studies of discharged electrode samples after formation are presented starting with the highest heating temperature of 300

https://dx.doi.org/10.1021/acs.chemmater.9b04355
Chem. Mater. 2020, 32, 1210−1223

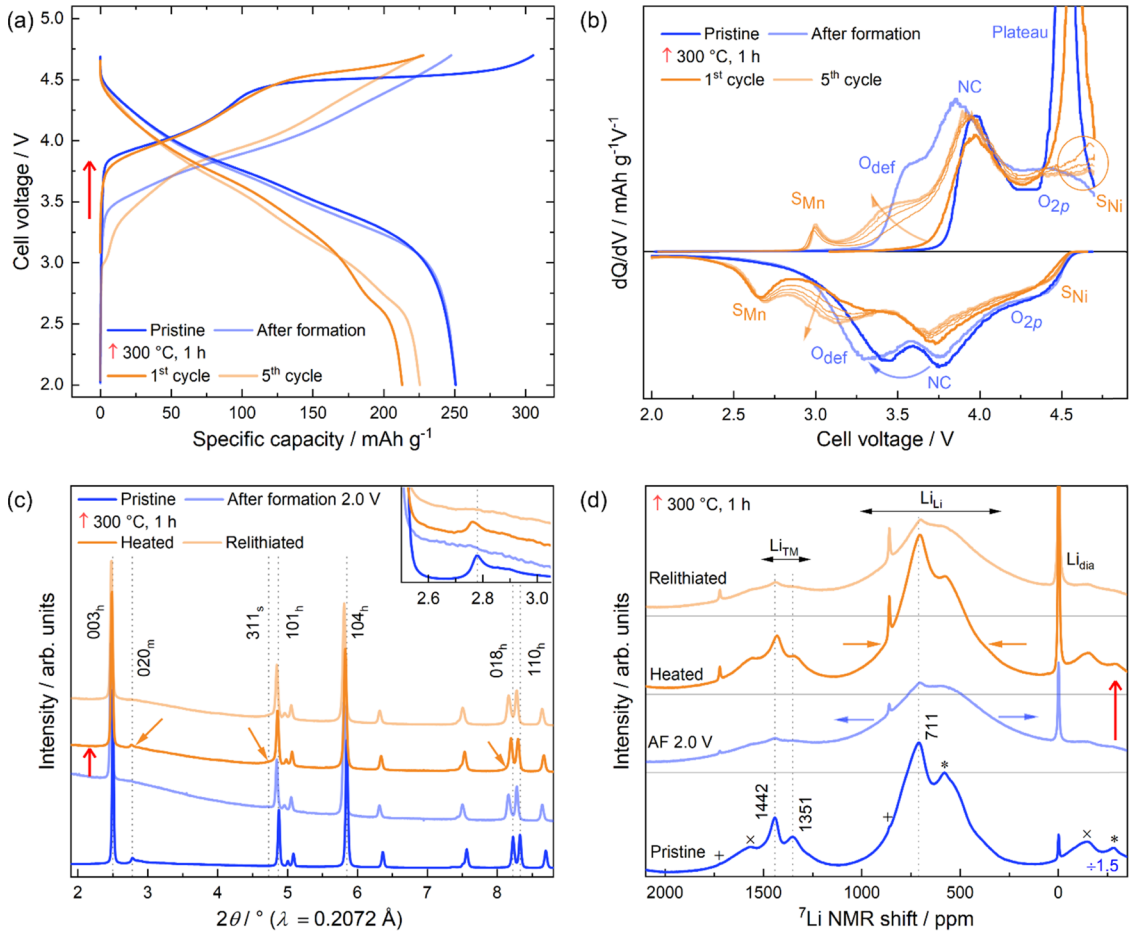

Figure 1. Thermal treatment of discharged samples (2.0 V): (a) cell voltage vs specific capacity and the corresponding differential capacity (dQ/dV) plot (b) between 4.7 and 2.0 V, (c) ex situ SRPD data with a magnification of the superstructure reflections in the inset and (d) ^{7}Li MAS NMR spectra, with the spinning sidebands (±861 ppm) marked by $^+$ (Li_{dia}), * (Li_{TM}), and ^{x} (Li_{Li}). AF, after formation. For presentation purposes, the intensity of the spectrum belonging to the pristine sample is downscaled by factor 1.5.

°C to highlight the impact on the structural and electrochemical properties. Figure 1a shows the cell voltage vs specific capacity of the formation cycle and the cycle after formation as well as the first and fifth cycles after the heating step (post-thermal). For emphasizing the occurring redox processes, the corresponding dQ/dV vs cell voltage plot is presented in Figure 1b. During the initial charge of the pristine material, the first peak located at about 4.0 V ("NC"), also found for conventional NCM materials, is supposedly attributed to the oxidation of the transition-metal ions Ni and Co from +II/+III states to +IV. Here, it should be noted that the true proportion of cationic and anionic contributions to the charge compensation and a full oxidation to +IV is still under debate.[2] To focus on the structure−property relationship of the material investigated in this work, the simplified assumption, including full oxidation of Ni and Co to +IV, was used. So far, the electrochemical delithiation (charging) process can be considered to be reversible and thus the initial state can be reached again by lithiating (discharging) the material.[24,25]

The second oxidation process with an extended plateau at 4.5 V corresponds to the irreversible formation process that is characteristic of Li- and Mn-rich NCMs. This induces a loss of the initial electrochemical and structural features, which is most clearly demonstrated by the disappearance of the charging plateau for further charge/discharge cycles as well as the loss of the short- and long-range atomic ordering as will be shown below in detail. The charge compensation of Li extraction during the plateau is carried out by the reversible as well as by the irreversible oxidation of oxygen, which leads to the partial release of oxygen from the surface and accompanied by a densification of the surface layer.[6,7]

Due to the electrochemically irreversible structural modifications in the bulk and surface, a reduction process corresponding to this plateau of the initial charging is no longer present. Instead, two newly occurring processes are present in addition to the reduction peak NC: (i) the reduction peak at around 4.3 V, which is commonly ascribed to the annihilation of electron holes in the oxygen 2p band ("O_{2p}"), which are formed during the charging plateau;[5,8,26] and (ii) the new low-voltage process at around 3.3 V, which was recently assigned to a reversible anionic $O^{2-/n-}$-contribution.[8,9,27] Interestingly, this anionic redox process exclusively appears in the Li-rich materials, and its emergence is obviously directly related to the initial formation process, which leads to a highly defective and metastable structure. Therefore, it is termed here as defect-related oxygen contribution "O_{def}".

At the end of discharge, an irreversible capacity loss of 54 mAh/g (first charge capacity of 305 mAh/g − first discharge capacity of 251 mAh/g) can be identified, which can be mainly attributed to the loss of electrochemically active lithium sites.[4]

https://dx.doi.org/10.1021/acs.chemmater.9b04355
Chem. Mater. 2020, 32, 1210−1223

In the second charging cycle, the onset voltage of the first oxidation peak is lowered to 3.3 V. It represents the newly formed reversible redox process O_{def}, continued by NC and O_{2p}. The same processes can be observed during the second discharge in a reversed order. The Li-rich cathode material reveals a decrease of the mean charge/discharge voltages with increasing number of cycles (voltage fade) as highlighted by the blue arrow. The low-voltage region O_{def} becomes more prominent at the expense of the high-voltage region NC, leading to a decrease of the mean voltage.

A discharged sample (2.0 V) after formation was heated at 300 °C for 1 h in an inert argon atmosphere, reinserted into a coin cell using a fresh electrolyte and a lithium metal anode, and electrochemically characterized for five further cycles (post-thermal). The most surprising observation emerging from the first post-thermal charge is the reoccurrence of the plateau at about 4.5 V and thus indicates the (partial) recovery of the initially well-ordered structure of the pristine material. Generally, the electrochemical features are very similar to the pristine material. The first oxidation process NC starts again at 3.7 V compared to 3.3 V for the sample after formation and is attributed to the oxidation of Ni and Co to +IV. Now, a less pronounced and shortened plateau in comparison to the pristine sample follows, leading to an overall charge capacity of 226 mAh/g. Analogous to the formation cycle of the pristine material, the plateau vanishes after the first post-thermal charge. Instead, the redox processes O_{def} and O_{2p} are active again in the following charge and discharge steps. Interestingly, the first post-thermal discharge and the following cycles show the additional redox process "S_{Mn}" at around 2.7/3.0 V (charge/discharge). As highlighted by the orange circle in Figure 1b, the second post-thermal charging curve as well as the following cycles after heat treatment reveals another newly arising oxidation peak "S_{Ni}" around 4.5−4.7 V. The corresponding reduction peak is probably strongly overlapping with the reduction peak O_{2p}. These findings strongly suggest the reversible de-/lithiation of a second phase, which has very similar electrochemical features as a $LiNi_{0.5}Mn_{1.5}O_4$ (LNMO)-type spinel.[28] As shown by the dQ/dV plot of the $LiNi_{0.5}Mn_{1.5}O_4$ reference in Figure S2, the high-voltage peak S_{Ni} is associated with the redox activity of $Ni^{2+/4+}$ and the low-voltage peak S_{Mn} with $Mn^{3+/4+}$. Later on, the formation of a second phase during the thermal treatment will be confirmed by diffraction measurements followed by a discussion on the underlying mechanism. As indicated by the orange arrows in the dQ/dV plot, region O_{def} develops a stronger contribution to the capacity (voltage fade) during the five post-thermal cycles and overcompensates the capacity loss in region NC. This leads to an increase of the discharge capacity from 213 to 225 mAh/g within five cycles.

Figure 1c shows the ex situ synchrotron radiation powder diffraction (SRPD) patterns of the pristine cathode powder as well as that of the samples after formation, heating, and relithiation (post-thermal cycles). For a detailed presentation of selected refined parameters from the Rietveld refinement and the underlying structural model, the reader is referred to the Supporting Information Section SI.3. Although the diffraction pattern of the pristine material clearly confirms the existence of monoclinic $C2/m$ superstructure reflections, a structural model based on the rhombohedral $R\bar{3}m$ symmetry was used for crystallographic simplicity and to emphasize the alteration of the refined structural parameters after the electrochemical cycling and the thermal treatment, respectively. The $C2/m$ superstructure reflections are weakly developed and predominantly represented by the 020_m reflection around 2.8° (2θ), with a gently sloping flank on the right side. This can be explained by variations of the stacking sequence (stacking faults) of the, in a (Li/TM)-TM_6 honeycomb scheme, highly ordered TM layers along the c-axis leading to an asymmetric "Warren-shaped" profile broadening.[29,30]

After the formation cycle, some clear changes are observed in the diffraction pattern, which are ascribed to the irreversible processes occurring at the plateau. First, the $C2/m$ superstructure reflections and thus the long-range (Li/TM)-TM_6 honeycomb ordering disappeared. Furthermore, a comparison of the half widths of the neighboring 018_h and 110_h reflections indicates a strong anisotropic lattice strain in the hexagonal c direction (variations of the c parameter). This anisotropic strain leads to a pronounced broadening of c-dependent reflections, e.g., the aforementioned 018_h reflection. The anisotropy might be induced by a nonhomogeneous relithiation of the material resulting in a different local density of Li atoms, either from grain to grain or even within a grain. The migration of transition metals from the TM to the Li layers was modeled by an exchange of Li and Ni between these layers. The refined Ni content in the Li layers increased from 0.8(3)% in the pristine sample to 4.7(6)% in the sample after formation. This suggests an irreversible migration of transition metals from the octahedral 3a sites of the TM layers to the octahedral 3b sites of the Li layers during the formation cycle.[31]

After heating the discharged sample after formation at 300 °C for 1 h, three major changes stand out in the diffraction pattern highlighted by the orange arrows. (i) The most striking observation is the reappearance of the $C2/m$ superstructure reflections as clearly apparent from the inset of Figure 1c. This finding explicitly points to the (partial) recovery of the long-range Li/TM-TM_6 honeycomb ordering. (ii) The half-width of the 018_h reflection is narrowed again, suggesting a reduction of the c-anisotropic lattice strain. (iii) Some reflections reveal a specious asymmetric broadening most clearly seen for the 110_h reflection. The structural analysis of the diffraction data reveals the origin of the "broadening" to be the formation of a nanocrystalline second phase, which can be assigned to a cubic spinel with space group $Fd\bar{3}m$. Since the exact composition of the newly formed phase cannot be derived from the data, the $LiMn_2O_4$ spinel was used for Rietveld refinement. The phase content of $LiMn_2O_4$ in the sample after heating was refined to 16(3)% (w/w) with an average apparent domain size of approximately 4 nm. After heating, a mass loss of 2.2(6)% (w/w) was determined for the electrode coating, which includes the active material, binder, and carbon. Furthermore, a contribution from the decomposition of DMC-insoluble electrolyte products on the cathode cannot be excluded at this point. Commonly, the observed mass loss in layered oxide cathode materials during heating is ascribed to oxygen release with a simultaneously occurring structural phase transition toward an oxygen-poor phase,[32] for instance, the observed spinel formation.

After the five post-thermal cycles (relithiation), similar changes appear in the diffraction pattern as already discussed for the diffraction pattern of the pristine sample after formation, including the disappearance of the $C2/m$ superstructure reflections (compare light blue and light orange lines in Figure 1c). However, the nanosized spinel is still present

https://dx.doi.org/10.1021/acs.chemmater.9b04355
Chem. Mater. 2020, 32, 1210−1223

[refined to 14(3)% w/w, 5 nm average apparent domain size], which is well in agreement with the reversible redox activity of an LNMO spinel represented by the redox peaks S_{Mn} and S_{Ni} in the electrochemical data.

As shown in Figure 1d, the ^{7}Li MAS NMR spectrum of the pristine cathode powder consists of three groups of lithium environments. The resonance around 0 ppm represents the diamagnetically embedded lithium Li_{dia}, e.g., LiOH, Li_2CO_3, components of the cathode electrolyte interphase (CEI), and/or residues of the electrolyte salt. The two paramagnetic groups between 300 and 1000 ppm and between 1300 and 1500 ppm belong to layered Li-rich transition-metal oxide structures.[4] They are assigned to lithium in the Li layers (Li_{Li}) and lithium in the TM layers (Li_{TM}), respectively. The isotropic ^{7}Li resonances are overlapping with several spinning sidebands from all three groups, which complicates the quantitative analysis especially for resonances at high shift values. For this reason, the NMR spectra are qualitatively discussed based on the evolution of: (i) the rather sharp peaks at 711, 1351, and 1442 ppm associated with well-defined Li coordinations in highly ordered environments; and (ii) the broad resonance ranging from 300 to 1000 ppm associated with a large variety of different Li environments similar to those in pure NCM.[4,33] The prominent peak at 711 ppm can be directly linked to Li in the Li layer within Mn-rich surroundings comparable to pure Li_2MnO_3. The peaks at 1351 and 1442 ppm can be assigned to the Li-Mn_5(Ni,Co)$_1$- and Li-Mn_6-type honeycomb cation ordering within the TM layer, respectively. A detailed deconvolution of the spectrum regarding the pristine Li- and Mn-rich cathode powder is presented in Section SI.3.

After formation ("AF 2.0 V"), the resonances are significantly broadened (blue arrows), due to the loss of local ordering. Associated therewith is the formation of many different Li environments particularly in formerly well-ordered Li_2MnO_3-like environments leading to a rather large variety of NMR shifts. The peaks at 1442 and 1352 ppm, which are associated with the local Li-TM_6 honeycomb ordering in the transition-metal layers, almost vanished. Again, the loss of the long-range ordering has already been proven by the disappearance of the *C*2/*m* superstructure reflections. Due to the rather high current rate and an upper cutoff voltage of 4.7 V, the small peak residues at 711 and 1442 ppm might be arising from electrochemically inactive regions, which are still in their pristine state. Whether the Li_{TM} sites remain primarily unoccupied after formation or whether their environment has changed considerably cannot be quantified here, since the Li_{TM} resonances strongly overlap with the spinning sidebands from the Li_{Li} resonances. ^{6}Li NMR measurements (Figure S6), using a fully ^{6}Li-enriched cell setup (electrolyte and lithium metal anode), suggest that the Li_{TM} sites are partially reoccupied after the first cycle. Previous quantitative ^{6}Li NMR studies from Dogan et al. suggest that less than half of the Li_{TM} sites and overall 87% of all initially available Li sites are relithiated at the end of the formation cycle, which agrees well with the observed irreversible capacity loss.[4]

Very interestingly, the thermal treatment of a discharged sample after formation led to a pronounced reappearance of the well-defined Li_{TM} resonances at 1442 and 1351 ppm, which are directly related to the Li-TM_6 honeycomb ordering in the TM layers. In conjunction with the intensification of the 711 ppm resonance, this clearly indicates the (partial) recovery of the well-ordered pristine state in the entire bulk material. In contrast to the results from the diffraction and electrochemical measurements, the NMR spectrum shows no direct evidence of the formation of a spinel phase. After the five post-thermal electrochemical cycles, the ^{7}Li NMR spectrum is again similar to that of the sample after formation, including the loss of local ordering and an overall peak broadening. Here as well, no direct indication for a lithiated spinel phase was found. The spectral features that can be ascribed to the spinel lithium sites are supposed to be "buried underneath" the broad Li_{Li} resonance of the layered phase.[4,34]

The so-far presented results strongly suggest the partial recovery of the pristine well-ordered state in a discharged sample after heating at 300 °C for 1 h. To get a more detailed picture concerning the reordering processes and the onset temperature of the spinel formation, the heating experiments were repeated at temperatures of 150, 200, and 250 °C. As apparent from the d*Q*/d*V* plot of the first post-thermal cycles in Figure 2, the peak area belonging to the defect-related

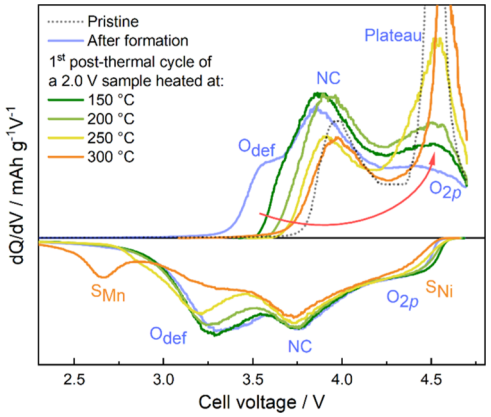

Figure 2. d*Q*/d*V* plot of the first post-thermal cycle of discharged samples (2.0 V) after heating at varying temperatures between 150 and 300 °C for 1 h.

oxygen contribution (O_{def}) is continuously declining with increasing temperature. Obviously, this process is directly correlated with the rising emergence of the plateau at 4.5 V. Below 300 °C, the restoration of the electrochemical features toward the initial pristine state is not linked to the formation of a redox active spinel phase, as suggested by the absence of the redox peaks S_{Mn} and S_{Ni}. This observation is further supported by the corresponding diffraction patterns (Figure S8), where no indication for the formation of a second phase is found below 300 °C. Instead, a gradual recovery of the local ordering can be observed as indicated by: (i) the continuous narrowing of the ^{7}Li NMR resonances (Figure S9), (ii) the decrease of the refined lattice parameters *a* and *c* toward the initial pristine values (Figure S10), (iii) the decrease of the lattice strain and its *c*-anisotropy, and (iv) a very weak reoccurrence of the 020_m superstructure reflection.

3.2. Thermal Treatment of Charged Samples (4.7 V).

As shown in Figure 3a,b, the thermal treatment (300 °C, 1 h) of a charged electrode after formation led to a strong degradation of the electrochemical properties, similar to those of highly cycled samples.[35] The first post-thermal discharge (red dotted line) is dominated by the low-voltage processes S_{Mn} and "S_{Mn2}", which again can be attributed to the lithiation of an LNMO-like spinel including an active $Mn^{3+/4+}$ redox couple. The discharge capacity significantly decreased

https://dx.doi.org/10.1021/acs.chemmater.9b04355
Chem. Mater. 2020, 32, 1210−1223

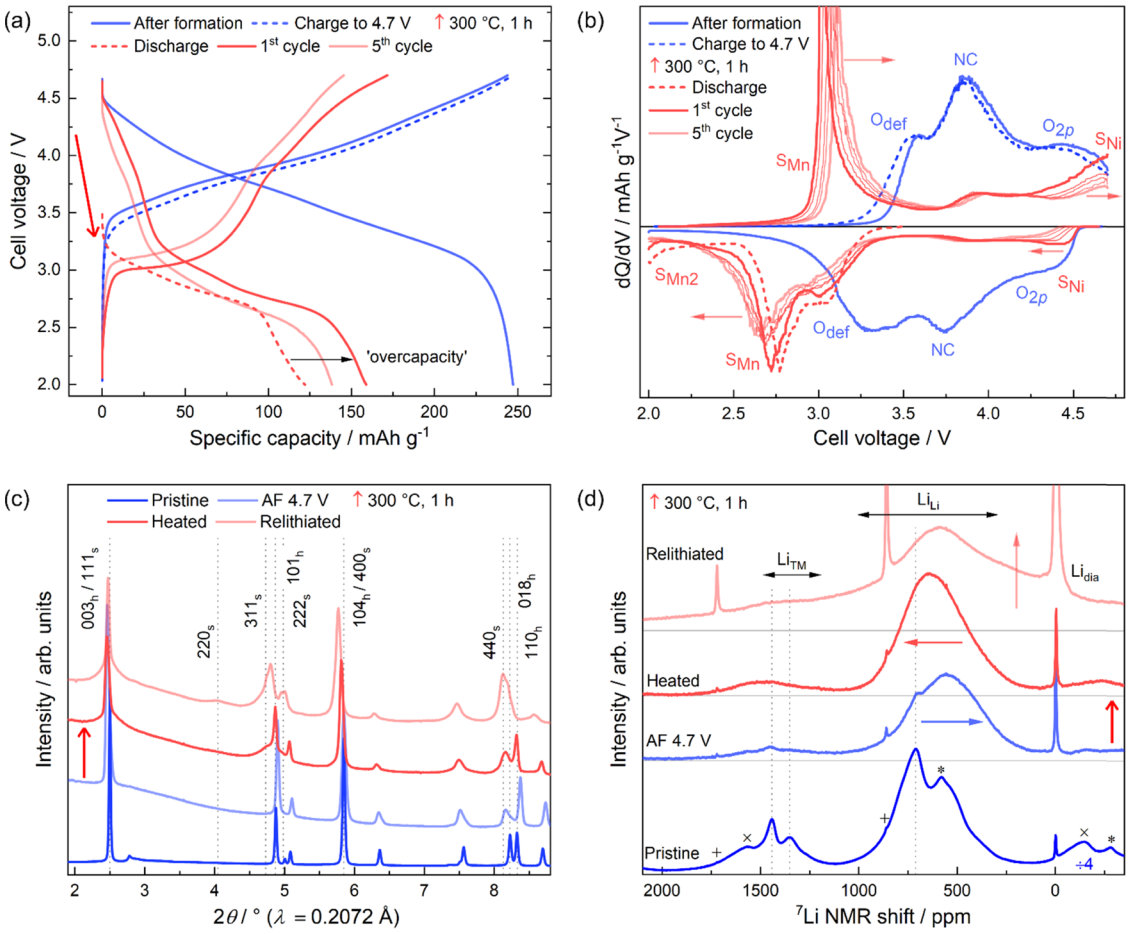

Figure 3. Thermal treatment of charged samples (4.7 V): cell voltage (a) and the corresponding differential capacity (dQ/dV) plot (b) between 2.0 and 4.7 V. Ex situ SRPD data (c) and ^{7}Li MAS NMR spectra (d), with the spinning sidebands (±861 ppm) marked by + (Li_{dia}), * (Li_{TM}), and ^{x} (Li_{Li}). AF, after formation. For presentation purposes, the intensity of the spectrum belonging to the pristine sample is downscaled by factor 4.

from 247 mAh/g before heating to 122 mAh/g after heating, which suggests a profound loss of electrochemically active Li sites after the thermal treatment.

The subsequent charging step begins with the oxidation peak S_{Mn} at a cell voltage of 3.0 V followed by a comparably weak oxidation peak at 3.9 V (NC) and one above 4.3 V (S_{Ni}), which were both absent in the preceding discharge step. Overall, a charge capacity of 171 mAh/g is reached, leading to an "overcapacity" of 49 mAh/g, since only 122 mAh/g was discharged (lithiated) beforehand. As is apparent from the dQ/dV plot, this overcapacity is mainly originating from the high-voltage region S_{Ni}, which is associated with the $Ni^{2+/4+}$ redox activity in an LNMO-like spinel. This observation is surprising, since there is no indication that nickel (+IV in the charged state) has been reduced within the first post-thermal discharge. Accordingly, nickel would be rather incapable of being oxidized in the subsequent charge. These findings lead to the conclusion that Ni must have been reduced from +IV to +II during the heating procedure. As described below, results of X-ray absorption spectroscopy support this conclusion by showing a clear shift of the Ni K edge toward lower absorption energies (reduction) after thermal treatment. To further evaluate the $Ni^{2+/4+}$ redox activity, a high-voltage extended dQ/dV plot until a charging voltage of 5.3 V is presented in Figure S2 in the Supporting Information. After five cycles, the electrode exhibits a continued decline of the charge and discharge capacity along with an increasing overpotential, as indicated by the divergence of the charge and discharge potential levels of the redox peaks S_{Mn} and S_{Ni} (highlighted by the red arrows). Results from post mortem energy-dispersive X-ray (EDX) spectroscopy of the lithium anode, used in the post-thermal cycling (Section SI.6), reveal the deposition of noteworthy amounts of TMs on the anode, predominantly Mn. This observation clearly points out the decomposition of the cathode sample and the dissolution of TMs into the electrolyte during post-thermal cycling. Since the disproportionation reaction of Mn^{3+} into Mn^{2+}/Mn^{4+} and the subsequent dissolution of Mn^{2+} into the electrolyte is a known degradation mechanism[36] for LNMO and LMO spinels, these findings further support the formation of spinel in the material during heating.

From the ex situ diffraction pattern of the charged sample after formation, cf. Figure 3c, it can be seen that the structural appearance of the charged material can still be well described with a rhombohedral $R3m$ setting. Thus, the delithiation itself does not induce a long-range alteration of the crystal structure, e.g., toward a lithium-poor phase. The even more pronounced broadening of the 018_h reflection in comparison to the discharged sample indicates an increase of the lattice strain along with a strong anisotropic component (variation of the c parameter) after the delithiation of the layered lattice.

After the thermal treatment of a charged sample at 300 °C for 1 h, clearly visible "shoulders" appeared at the 003_h and the 101_h reflection. These shoulders can be well-ascribed to the

https://dx.doi.org/10.1021/acs.chemmater.9b04355
Chem. Mater. 2020, 32, 1210−1223

111_s and the 311_s reflection of a second nanosized spinel phase, which were already observed to a lower extent in the diffraction patterns of discharged samples after heating. The phase content of $LiMn_2O_4$ was refined to 49(5)% (w/w) and further increased to 64(4)% (w/w), after the material had been relithiated. The average apparent domain sizes were refined to approx. 5 nm. A detailed analysis of the refined parameters (results shown in Figure S14) clearly indicates the tendency toward a more spinel-type cation arrangement also in the still layered $R\bar{3}m$ phase after heating. The determined occupancy of Ni in the Li layers increased from 4.7(6)% before heating to 15.4(9)% after heating, suggesting a profound migration of transition metals from the TM into the Li layers. This value is maintained after relithiation, which emphasizes the irreversible character of this process.

Interestingly, the determined lattice parameter *a* of the layered $R\bar{3}m$ phase increases from 2.8358(3) Å before heating to 2.8545(4) Å after heating, which is very close to the pristine value of 2.8548(1) Å. Since the increase of *a* is an indicator of expansion of the TM ion radii and thus the reduction of their oxidation states, this finding might suggest the reduction of the TMs during the thermal treatment, most probably to a similar configuration of the oxidation states as in the pristine material: Ni(+II), Co(+III), Mn(+IV). The relithiation of the heated electrode even led to a further increase of the lattice parameter *a* to a value of 2.8921(4) Å, which is far beyond that of the pristine material. Presumably, this could be induced by the partial reduction of manganese from +IV to +III. These findings are well in agreement with the electrochemical results, where the reduction of nickel during the heat treatment was proposed as well as the subsequent reduction of Mn during relithiation.

A closer look at the 222_s and 400_s reflections reveals that these show a much lower size-induced broadening than the 111_s and 311_s reflections for example. Interestingly, these narrower reflections are strongly related to the oxygen sublattice. To include this observation in the structural model, the profiles of the oxygen-associated reflections were refined individually with a Lorentzian-type broadening. The extended model led to an improvement of the fit quality and is discussed in detail in Section SI.3. These results can be interpreted by the local formation/nucleation of nanosized domains with a spinel-type cation arrangement, which are coherently embedded within a continuous oxygen matrix. The nanodomains and the matrix share the same cubic closed packed (ccp) oxygen sublattice, which explains the absence of a size-induced broadening in the oxygen-associated reflections.

As shown in Figure 3d, the ^{7}Li MAS NMR spectrum of the charged sample after formation is dominated by the broad Li_{Li} resonance, indicating an (almost) complete delithiation of the TM layers. The center of this group moved from 615 ppm in the discharged state toward lower values of around 555 ppm in the charged state as highlighted by the blue arrow. This observation can be explained by the oxidation of nickel to the diamagnetic +IV state and/or the diffusion of lithium from octahedral into tetrahedral sites.[37] Just like in the spectrum of the discharged sample (cf. Figure 1d), two residual Li_2MnO_3-like peaks at 711 and 1442 ppm are still identifiable, very likely due to EC-inactive regions in the active material. After the heat treatment, the Li_{Li} resonance group moves back toward higher NMR shifts of approximately 630 ppm, which is probably related to the reduction of Ni ions toward on oxidation state of +II. Moreover, the almost symmetric and featureless appearance of the signal might be an indicator of a more random distribution of the surrounding transition metals.[38] However, whether the remaining Li ions are occupying octahedral sites in a still layered-type environment or whether they have migrated to tetrahedral sites in a cubic spinel-type environment during the thermal treatment cannot be deduced from the data. At least a distinct composition, e.g., of an ordered and well-crystallized $LiNi_{0.5}Mn_{1.5}O_4$ or $LiMn_2O_4$ spinel can be excluded at this point, since these would appear as a rather sharp resonance at 925 or 520 ppm, respectively.[39] Furthermore, the signals at 711 ppm and 1442 ppm are absent in the sample after heating, pointing out the dissolution of the aforementioned Li_2MnO_3-like residues.

Interestingly, the spectrum of the relithiated sample features a broad "bump" at around 250 ppm as highlighted by the vertical arrow. Due to the broad character, a distinct allocation of the newly formed Li environment(s) is difficult. Two possible explanations might be: (i) the occupancy of octahedral 16*c* sites in a spinel, which was already observed for overlithiated LNMO[40] and LMO[39,41] as well as for activated Li_2MnO_3,[42] and/or (ii) the occupancy of under-coordinated tetrahedral sites (CN < 4) due to oxygen vacancies in a still maintained layered framework.[14] Moreover, the spectrum shows a significant increase and broadening of the signal around 0 ppm, which is associated with lithium embedded in a diamagnetic environment, for instance, DMC-insoluble reaction products from the electrolyte.

To get a more detailed insight into the layered-to-spinel transformation process, the experiments were repeated at 150 °C, 200 °C, and 250 °C. Figure 4 shows the d*Q*/d*V* plot

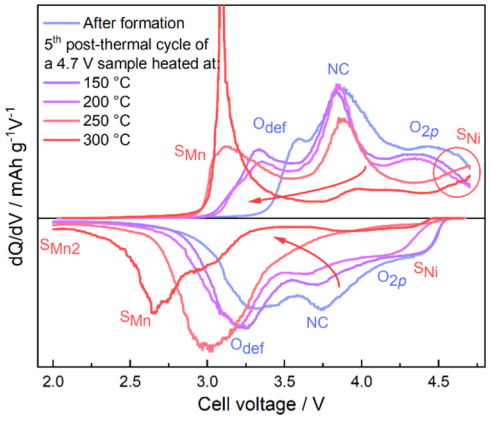

Figure 4. d*Q*/d*V* plot of the fifth post-thermal cycle of charged samples (4.7 V) after heating at varying temperatures between 150 and 300 °C for 1 h.

regarding the fifth post-thermal cycles. From the data, it is apparent that the electrochemical degradation intensifies with increasing temperature: the area of the O_{def} peak increases gradually at the expense of the higher-voltage regions NC and O_{2p} (voltage fade), and the redox peaks associated with an LNMO-like spinel appear, starting from a temperature of 250 °C.

Generally, from the results of the Rietveld refinement (Figure S14), it is evident that the electrochemical characteristics directly correlate, for instance, with the refined spinel phase content and the refined occupancy of Ni in the Li layers. Up to a heating temperature of 200 °C, no spinel phase could be refined for the diffraction patterns of the relithiated samples.

https://dx.doi.org/10.1021/acs.chemmater.9b04355
Chem. Mater. 2020, 32, 1210−1223

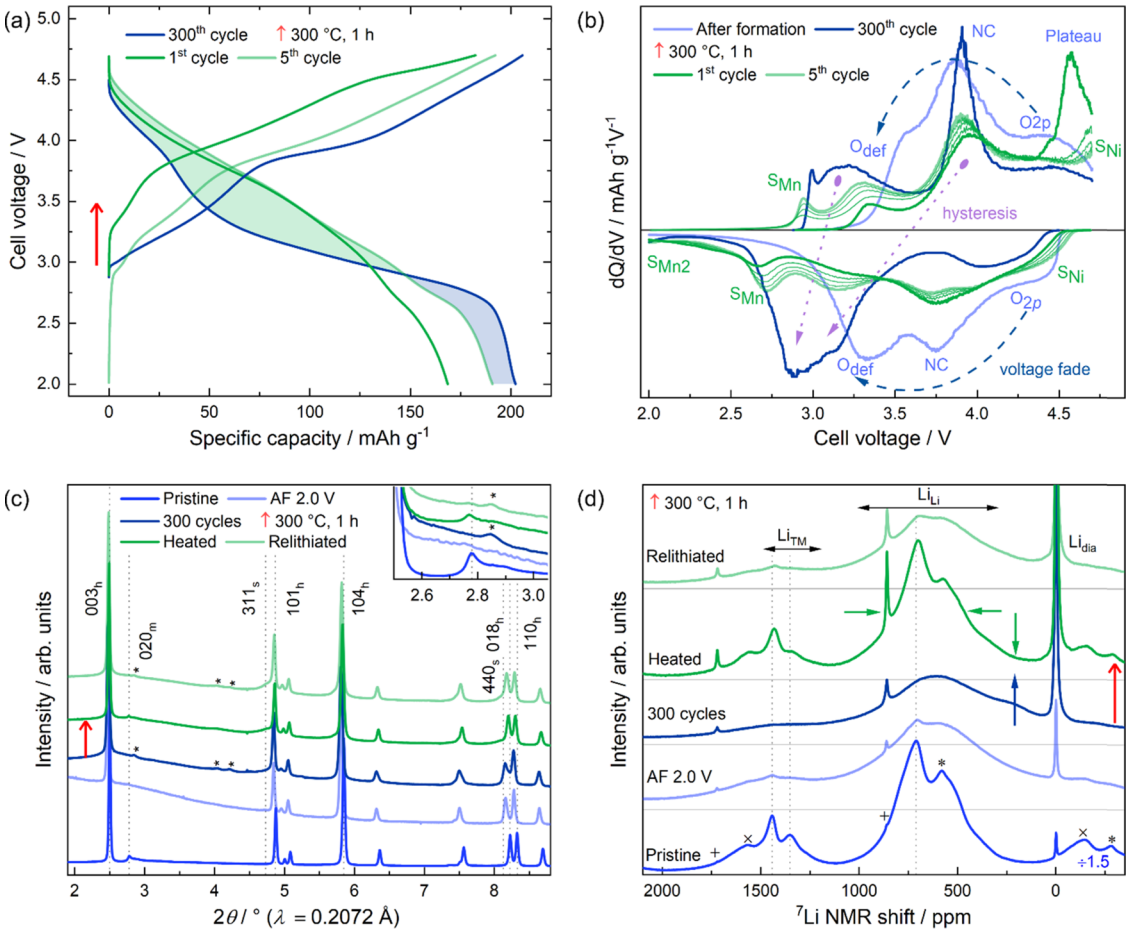

Figure 5. Thermal treatment of fatigued samples (300 cycles): cell voltage (a) and the corresponding differential capacity (dQ/dV) plot (b) between 2 and 4.7 V. Ex situ SRPD data (c) with a magnification of the superstructure reflections in the inset (* Li_2CO_3) and ^7Li MAS NMR spectra (d), with the spinning sidebands (±861 ppm) marked by $^+$ (Li_{dia}), * (Li_{TM}), and ^{x} (Li_{Li}). For presentation purposes, the intensity of the spectrum belonging to the pristine sample is downscaled by factor 1.5.

For the 250 and 300 °C samples, spinel contents of 23(5) and 64(4)% (w/w) were determined. These results are well in agreement with the appearance of the spinel-related redox peaks in the corresponding dQ/dV curves at 250 °C and above. Importantly, these structural changes are well related to the mass loss of the electrode coating (active material, binder, carbon) after heating. Whereas up to 200 °C almost no mass loss (<1% w/w) could be determined, the value increases remarkably for the 250 °C sample to 3.3(6)% and for the 300 °C sample to 9.9(7)% (w/w).

3.3. Thermal Treatment of Electrochemically Fatigued Samples (300 Cycles). As can be clearly seen from Figure 5a, the extensive cycling of a Li- and Mn-rich NCM resulted in a pronounced voltage and capacity fade. The discharge capacity dropped from 251 mAh/g after formation to 202 mAh/g after 300 cycles, the mean discharge voltage from about 3.6 to 3.2 V, respectively. In the corresponding dQ/dV vs cell voltage plot in Figure 5b, the voltage fade (dashed arrows) and the hysteresis (dotted arrow) are highlighted. The contribution of the low-voltage redox processes O_{def} and S_{Mn} increases at the expense of the high-voltage process O_{2p}, leading to a decrease of the mean charge/discharge voltage (voltage fade). Whereas in the charging step the oxidation peaks O_{def} and NC are clearly separated, the reduction peak NC completely shifts inside the area of the reduction peak O_{def} in the discharge step. This leads to a charge/discharge voltage difference of the redox peak NC of about 0.8 V and thus to a pronounced hysteresis and energy inefficiency. After 300 cycles, the spinel-associated redox peak S_{Mn} emerged, which may be indicating an active redox activity of Mn. However, in contrast to the thermally fatigued samples, the high-voltage redox peak S_{Ni} is not identifiable.

Analogous to the experiments presented above, the electrochemically fatigued electrode was thermally treated at 300 °C for 1 h. Most surprisingly, also the highly fatigued Li-rich material partially regenerated toward the pristine state, as evident from the first post-thermal cycle. The oxidation peaks S_{Mn} and O_{def} are significantly damped in comparison to the cycle before heating and the plateau reoccurs. This observation already indicates the recovery of the highly ordered state. However, the plateau is less pronounced than in the first post-thermal charge of the discharged sample after heating (cf. Figure 1d). Another very remarkable finding is the significant intensification of reduction peaks O_{2p} and NC in the subsequent discharge step in comparison to the fatigued sample. This is directly correlated with the damping of the low-voltage regions O_{def} and S_{Mn}. In other words, the pronounced voltage fade and hysteresis developed during extensive cycling have been partly reversed by the thermal treatment. Again, the partial recovery of the pristine properties is directly connected with the formation of an LNMO-like spinel, as is apparent from the rise of the spinel-related redox processes S_{Mn} and S_{Ni}.

https://dx.doi.org/10.1021/acs.chemmater.9b04355
Chem. Mater. 2020, 32, 1210−1223

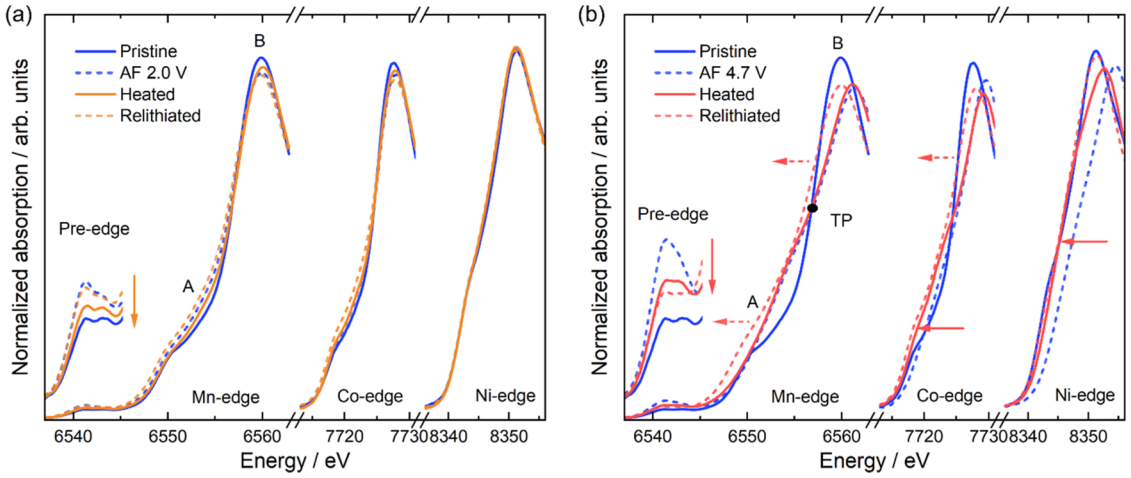

Figure 6. XANES spectra of the Mn, Co, and Ni K edges corresponding to the thermal treatment experiments of discharged (a) and charged (b) samples. The pre-edges of the manganese spectra are magnified in the inset. AF, after formation. TP, turning point.

After the five post-thermal cycles, two modifications are apparent in the dQ/dV plot: (i) the redox activity in the NC area decreases again and is intensified in the O_{def} region (voltage fade), and (ii) the redox activity of the spinel phase increases within the five cycles, as clearly indicated by the expansion of the area S_{Mn}. Overall, this leads to an increase of the discharge capacity from 169 mAh/g in the first to 191 mAh/g in the fifth post-thermal cycle. Furthermore, the mean discharge voltage increased to 3.4 V in comparison to 3.2 V for the fatigued sample as highlighted by the dyed areas in Figure 5a.

The data obtained from the diffraction measurement of the cycled sample is presented in Figure 5c. The diffraction pattern reveals a general broadening of the reflections in comparison to the pattern of the sample after formation. Especially the emergence of the 311_s reflection already indicates the partial transformation of the sample to a spinel. The Rietveld refinement (results are shown in Figure S15) revealed a spinel phase content of 34(16)% (w/w) with an average apparent domain size of about 2 nm, which indicates a very fine dispersion of these spinel domains in the layered matrix. Furthermore, the refinement disclosed a high lattice strain and a strong c-anisotropy of the lattice strain in the $R\bar{3}m$ matrix, which is also indicated by the broadened 018_h reflection. This suggests a large variety of locally different degrees of lithiation and probably cation arrangements as well as the loss of electrochemically active lithium sites due to the high degree of disorder in the material.

After the heating procedure, the $C2/m$ superstructure reflections reappear and the 018_h reflection narrows. The Rietveld refinement provides a spinel content of 21(7)% (w/w) with an apparent domain size of 3 nm, suggesting that within the range of error no additional material was converted to spinel during heating. This finding is surprising, since a mass loss of about 5(1)% was determined for the electrode and therefore suggests the loss of oxygen and the formation of an oxygen-poor phase during the thermal treatment. The overall lattice strain and its c-anisotropy decreased to values close to those determined for the sample after formation, which indicates a pronounced reorganization of the cations to reduce lattice strain. This reorganization process probably also includes a more pronounced segregation of the material into a lithium- and oxygen-rich pristine-like and a lithium- and oxygen-poor spinel phase. After five post-thermal cycles, the 020_m superstructure reflection vanishes again, indicating the loss of the long-range (Li/TM)-TM_6 honeycomb ordering. The spinel phase content was refined to 27(5)% (w/w) with an average apparent domain size of 4 nm.

The ^{7}Li NMR spectrum of the electrochemically fatigued sample (300 cycles) shown in Figure 5d reveals three prominent spectral changes in comparison to the spectrum of the sample after formation: (i) all resonances associated with the Li_2MnO_3-like Li environments (711, 1351, 1442 ppm) disappeared, indicating a complete formation and the loss of Li-TM_6 ordering; (ii) a newly formed broad resonance appeared at around 250 ppm as highlighted by the blue arrow; and (iii) the signal at 0 ppm, which represents the diamagnetically embedded lithium L_{dia}, increased in intensity noteworthily. Most surprisingly, a bump at around 250 ppm and an increase of the 0 ppm peak area were also observed in the spectrum belonging to a charged electrode after heating and relithiation as shown in Figure 3d. To emphasize the common features of both spectra, they are superimposed in Figure S16. This observation suggests a rather similar local Li environment in both samples. These findings are very interesting, since both samples share similar features, e.g., a pronounced spinel contribution to the electrochemical properties and a trend toward a more spinel-type cation arrangement in the ccp oxygen sublattice. However, as it is demonstrated now, the electrochemically fatigued sample still reveals the ability to restore the pristine ordering. Most probably, this restoration is possible due to the still intact oxygen sublattice, which suggests no profound bulk oxygen loss during cycling.

Notwithstanding the profound structural and electrochemical degradation, the heat treatment of the fatigued sample led to an almost entire recovery of the pristine local ordering. As can be clearly seen from the ^{7}Li NMR spectrum (see the dark-green line in Figure 5d), the resonances associated with the Li-TM_6 honeycomb ordering (1351 ppm and 1442 ppm) in the transition-metal layers reappear, which is well in agreement with the return of the $C2/m$ superstructure reflections as shown before. In addition, the 711 ppm resonance, which represents the Li_2MnO_3-like Li environments in the Li layers, is present again. Interestingly, the bump at 250 ppm vanished (green arrow) and did not reappear after the post-thermal cycles. Obviously, the Li environments, which are

https://dx.doi.org/10.1021/acs.chemmater.9b04355
Chem. Mater. 2020, 32, 1210−1223

observable at low shift values around 250 ppm (bump), might be linked to a decrease of the mean charge and discharge voltages (voltage fade). After the subsequent five post-thermal cycles, the spectrum is broadened again and the sharp signals, which are linked to a high degree of local ordering, vanished.

3.4. X-ray Absorption Spectroscopy. To study the element-specific changes of oxidation states and the local structural environments of the transition-metal ions during the thermal treatment experiments, hard X-ray absorption spectroscopy (XAS) was performed at the Mn, Co, and Ni K edges. Figure 6 shows the normalized X-ray absorption near-edge structure (XANES) spectra acquired after the thermal treatment experiments on discharged (2.0 V) and charged (4.7 V) samples. The spectra belonging to the electrochemically fatigued samples as well as a detailed analysis of the extended X-ray absorption fine structure (EXAFS) oscillations are presented in Sections SI.9 and SI.10. Additionally, surface- and bulk-distinguishing soft-XAS measurements concerning the oxygen K edge are shown in Section SI.11. The transition-metal K edge can be divided into three different edge features: the pre-edge region, the edge region "A", and the white line "B". The weak pre-edge peak is associated with formally forbidden electric dipole transitions from TM 1s to TM 3d orbitals for transition-metal ions located in an ideal octahedral environment. With increasing distortion of the octahedral framework and the occupation of tetrahedral sites (both leading to a 3d−4p orbital mixing), the 1s to 3d transition gets more and more allowed and the pre-edge peak appears in the spectra. Moreover, a depletion of *d* electrons leads also to an intensification of the pre-edge peak.[43] Region A represents the TM 1s to 4p electron transition combined with a ligand-to-metal charge transfer (shake-down) process, and the white line B represents the direct TM 1s to 4p transition. An oxidation of a TM ion accompanied by a loss of d electrons, for instance, is generally observable by a shift of the edge toward higher energies.

By comparing the spectra of the Li-rich material in the pristine state (blue line) and discharged after formation (dashed blue line) shown in Figure 6a, it can be concluded that the formation process induces no considerable shifts of the edge energies. This observation suggests similar oxidation states for all TMs in both states in the bulk. However, the increase of the Mn pre-edge intensity indicates an increased distortion of the octahedral symmetry and/or a potential migration of Mn ions to tetrahedral sites. These findings support the clear trend toward a lower degree of ordering on a local atomic scale in the samples after formation, as already exemplified before by the detailed analysis of the NMR data (cf. Figure 1d). Likewise, the decline of the Mn pre-edge intensity after heating (highlighted by the orange arrow) suggests the partial recovery of the initial pristine octahedral symmetry and probably the restoration of the (Li/TM)-TM_6 honeycomb ordering within the TM layers. After the five post-thermal cycles, the pre-edge intensity is increased again. Interestingly, after the post-thermal cycles, a significantly lower pre-edge intensity was found in the surface-representing data set (TEY mode) of the oxygen K edge (Figure S20) in comparison to the bulk-representing data (FY mode). This finding suggests the reduction of TM ions on the surface below the pristine oxidation state values and thus a partial reduction of Mn to +III, which is in good agreement with the observed $Mn^{3+/4+}$ redox activity in the electrochemical data (Figure 1b).

As can be seen from Figure 6b, the charging of an electrode after formation to 4.7 V leads to an obvious shift of the Ni K edge toward higher energies and thus to an oxidation from +II to +IV. In contrast, no clear shift of the manganese edge as a whole is observed after charging, but instead an alteration of the edge shape is observed. In fact, this modification can be described as a kind of torsion around the turning point "TP". Oishi et al. demonstrated[44] that the torsion of the Mn edge is not linked to the increase of the oxidation state by comparing the results from Mn K and L edge (2p to 3d transition) absorption spectra. Instead, these observations in the Mn K edge are mainly attributed to variations of the local environment during lithium de-/intercalation. The significant rise of the pre-edge intensity at increased states of delithiation suggests a highly distorted Mn-O_6 octahedron and/or the partial migration of Mn ions to tetrahedral sites. The Co K edge spectrum does not show a shift of the entire edge after charging to 4.7 V. This observation suggests a modification of the local environment in combination with or even without a change of the oxidation state.[45]

After the heating step (Figure 6, compare the blue dashed line with the red solid line), the Ni edge shifts back to its position in the pristine state, indicating a reduction of the Ni ions from +IV to +II. Furthermore, the low-energy region A of the Co edge shows a slight shift to lower energies, whereas the position of the white line B is unaffected. This observation provides no direct evidence of a change of the oxidation state. Nevertheless, a comparison with the spectrum of a Co_3O_4 spinel reference (Figure S17a) suggests the reduction of cobalt to a mixed valence state ($Co^{2+}/2Co^{3+}$) and the occupation of tetrahedral 8a sites with Co^{2+} ions, i.e., a M_3O_4-type spinel cation ordering ($Fd\bar{3}m$).[46] As a complementary remark, the occupation of these 8*a* sites with TMs can also be observed in the diffraction pattern by the emergence of the 220_s reflection (cf. Figure 3c). Aside from the decrease of the pre-edge intensity, surprisingly no significant changes of the Mn K edge can be identified. Overall, these findings correlate well with the determined mass loss of the sample after heating, the therewith associated oxygen loss, and the structural transition from initially layered to a spinel-type structure. Finally, the immense release of oxygen leads to the reduction of Ni and Co.

The subsequent five post-thermal cycles ending with a discharge to 2.0 V (relithiation; compare red and red-dashed lines) lead to a shift of the manganese K edge toward lower energies beyond the turning point TP, which suggests a partial reduction of the Mn ions and therefore an active Mn^{3+}/Mn^{4+} redox couple (cf. redox process S_{Mn}, Figure 3b).

4. DISCUSSION

4.1. Formation: Order−Disorder Transition. First publications, which studied the mechanisms involved in the initial formation cycle, also referred to as activation of Li−Mn-rich NCMs,[47,48] suggested an irreversible loss of bulk oxygen when charging above 4.4 V. This process is exemplified for pure Li_2MnO_3 in eq 1

$$Li_2MnO_3 \xrightarrow{>4.4V} 2Li^+ + 2e^- + MnO_2 + 1/2O_2\uparrow \quad (1)$$

This "classical activation model" would lead to the following consequences. First, there will be an irreversible migration of TM ions into former Li_{TM} sites and the release of oxygen from the surface, i.e., the densification of the entire lattice including bulk and surface. This "densified" lattice is supposed to be

https://dx.doi.org/10.1021/acs.chemmater.9b04355
Chem. Mater. 2020, 32, 1210−1223

isostructural to a non-Li-rich layered oxide, e.g., $LiCoO_2$. Second is the formation of $LiMnO_2$ in the subsequent discharge step and the activation of the $Mn^{3+/4+}$ redox couple. This hypothesis is in strong contrast to the findings obtained in this work. The thermal treatment of discharged samples after formation (2.0 V) as well as of electrochemically fatigued samples clearly demonstrated that the pristine well-ordered structural arrangement including a pronounced (Li/TM)-TM_6 honeycomb ordering can be partially recovered on a very local and on a long-range atomic scale. In contrast to eq 1, these findings strongly imply that the majority of the material still contains the initial oxygen content after the activation cycle as well as the absence of a profound migration of TM ions into former Li_{TM} sites (densification). This accords well with earlier publications, which showed that only a small proportion of the classically proposed amount of oxygen is actually released from the material[5,6] and mainly affects the surface layer, leaving behind a two-phase core-/shell-like material.[7,49,50] This "activated" modification possesses less active lithium sites, which cannot be refilled back to the pristine level during discharge even in a lithium anode half-cell configuration. Bearing in mind the two-phase model, the loss of active lithium sites can be explained by the densification of the surface layer as well as by the loss of ordering within the bulk.

According to the findings obtained in this work, the activation directly corresponds to the electrochemically irreversible breakup of the (Li/TM)-TM_6 honeycomb ordering on a long-range as well as on a very local atomic scale. Thereupon, a highly defective metastable structure is formed, which features the tendency toward a more spinel-type cation arrangement with increasing number of cycles. The initial deordering process leads to the emergence of a reversible anionic contribution to the charge compensation at low redox potentials, in this study termed defect-related oxygen contribution O_{def}. The heat treatment of discharged samples after formation clearly demonstrates the gradual suppression of this redox process O_{def} after the thermal treatment with increasing temperature. According to the structural investigations, this is linked to the gradual recovery of the initial binding conditions and therefore to the restoration of the initial electronic structure, leading to the reappearance of the plateau at a cell voltage of 4.5 V. However, due to the irreversible capacity loss in the initial formation cycle and thus a lower lithium content in the active material, a full recovery of the entire material cannot be achieved. This deficiency is compensated by phase separation at a heating temperature of 300 °C: the formation of a pristine-like Li-rich phase and a nanosized Li-poor LNMO-like spinel phase. As suggested by the surface-/bulk-distinguishing oxygen K edge measurements, this phase separation might be explained by an intensification of the two-phase core-/shell-like behavior, where the coexistence of a spinel and a layered component can be clearly identified.

4.2. Spinel Formation and Oxygen Loss. The investigations on the thermal treatment of charged electrodes (4.7 V) demonstrated a profound degradation toward a spinel-type cation arrangement associated with the loss of oxygen. Especially from the results of the TM K edge XAS measurements, it is apparent that after heating, the oxidation states of the TM ions are reduced toward the pristine configuration (Ni^{2+}, Co^{3+}, Mn^{4+}) along with the compensation of electron holes on the oxygen. Again, it should be noted that the true proportion of cationic and anionic contributions to the charge compensation is still under debate. Therefore, only a semiquantitative estimation of the oxidations states was carried out, after each step, to summarize and illustrate the identified well-matching observations in a coherent picture. The oxygen release process during heating can be described by eq 2 as follows:

$$\overset{+1}{Li_{0.25}}\overset{+4}{Mn_{0.55}}\overset{+4}{Ni_{0.15}}\overset{+4}{Co_{0.1}}\overset{-1.45}{O_2} \xrightarrow{300\ ^\circ C} \overset{+1}{Li_{0.25}}\overset{+4}{Mn_{0.55}}\overset{+2}{Ni_{0.15}}\overset{+3}{Co_{0.1}}\overset{-2}{O_{1.53}} + 0.24\overset{0}{O_2}\uparrow \quad (2)$$

where the presumed Li content per formula unit is based on the electrochemical data neglecting side reactions. The thereof derived amount of released oxygen fits well to the estimated values being based on the electrode mass loss after heating, where an oxygen loss of 0.22 or 0.3 O_2 per formula unit can be derived by assuming O_2 or CO_2 as degassing species (Table S1). The thus-obtained oxygen loss leads to an O/TM ratio smaller than 2, indicating a full densification toward a $LiTMO_2$-type layered and/or $LiTM_2O_4$-type spinel cation arrangement. Since Ni and Co are probably already in their +II/+III state, the first post-thermal discharge includes the reduction of manganese, as emphasized by eq 3

$$\overset{+1}{Li_{0.25}}\overset{+4}{Mn_{0.55}}\overset{+2}{Ni_{0.15}}\overset{+3}{Co_{0.1}}\overset{-2}{O_{1.53}} \xrightarrow{\text{discharge to 2.0 V } +0.4Li} \overset{+1}{Li_{0.65}}\overset{+3.3}{Mn_{0.55}}\overset{+2}{Ni_{0.15}}\overset{+3}{Co_{0.1}}\overset{-2}{O_{1.53}} \quad (3)$$

This process leads to an active $Mn^{3+/4+}$ redox couple, which is identifiable as well in the following cycles at a cell voltage of around 3.0/2.7 V (ox/red) in the corresponding dQ/dV plot and is rather similar to the low-voltage plateau in LMO- or LNMO-type spinels. The related dissolution of Mn^{2+} into the electrolyte and the strong capacity fade provided further evidence of Mn redox activity. In the subsequent delithiation step (charge), first Mn^{3+} is oxidized to Mn^{4+}, followed by the high-voltage redox activity of Ni as presented by eq 4

$$\overset{+1}{Li_{0.65}}\overset{+3.3}{Mn_{0.55}}\overset{+2}{Ni_{0.15}}\overset{+3}{Co_{0.1}}\overset{-2}{O_{1.53}} \xrightarrow{\text{charging up to 4.7 V } -0.55Li} \overset{+1}{Li_{0.1}}\overset{+4}{Mn_{0.55}}\overset{+3}{Ni_{0.15}}\overset{+3}{Co_{0.1}}\overset{-2}{O_{1.53}} \quad (4)$$

Since there is still 0.1 Li left per formula unit and not all TMs are fully oxidized, the material can be further reversibly delithiated up to 5.3 V as illustrated by eq 5

$$\overset{+1}{Li_{0.1}}\overset{+4}{Mn_{0.55}}\overset{+3}{Ni_{0.15}}\overset{+3}{Co_{0.1}}\overset{-2}{O_{1.53}} \xrightarrow{\text{charging up to 5.3 V } -0.1Li} \overset{+1}{Li_0}\overset{+4}{Mn_{0.55}}\overset{+3.7}{Ni_{0.15}}\overset{+3}{Co_{0.1}}\overset{-2}{O_{1.53}} \quad (5)$$

Most probably, this high-voltage activity is originating from the delithiation of tetrahedral sites and the oxidation of Ni, rather similar to the LNMO-type spinel. The gradual increase of the heating temperature clearly showed the correlation of oxygen release and spinel formation. Up to 200 °C, no significant mass loss was determined after heating and the corresponding dQ/dV curves revealed no spinel contribution during charge/discharge, but the mean charge/discharge voltage decreased (voltage fade), which may be originating from the very local cation rearrangement during heating. From 250 °C on, the spinel phase emerges in the electrochemical as well as in the diffraction data along with a determined mass loss of the electrode, which emphasizes the direct link between the irreversible cation rearrangement in a spinel-type manner and the loss of oxygen.

https://dx.doi.org/10.1021/acs.chemmater.9b04355
Chem. Mater. 2020, 32, 1210−1223

4.3. Degradation Processes in Highly Cycled Cathode Samples. Continuous cycling results in unwanted voltage fade and increase of hysteresis attributed to a local cation rearrangement, which is clearly apparent from the electrochemical and structural investigations of the electrochemically fatigued sample (300 cycles). For example, this is demonstrated by the emergence of a nanosized spinel phase (cf. Figure 5c) and the increase of the refined lattice strain as well as the appearance of new Li environments in the ^{7}Li NMR spectra (Figure 5d). The analysis of the diffraction data reveals a significant amount of nanosized spinel that, for instance, was also determined for the samples heated in the charged state (4.7 V) at a temperature of 250 °C and above. But interestingly, the electrochemical behavior differs considerably from these thermally fatigued samples. The spinel-associated redox peaks S_{Ni} and S_{Mn} are not clearly identifiable in the dQ/dV curve of the 300th cycle (Figure 5b), but rather an intensification of the low-voltage redox process O_{def} is apparent. The Mn K edge of the fatigued sample shows no shift of the entire edge and therefore does not support a significant $Mn^{3+/4+}$ redox activity in the bulk (cf. Figure S17). Overall, this seems to be rather contradictory to the analysis of the diffraction data, i.e., a clear structure−electrochemical property relationship is not apparent. One possible explanation will be discussed next.

After heating an electrochemically fatigued sample at 300 °C for 1 h (cf. Figure 5), the pristine well-ordered state is partially recovered, as demonstrated by the reappearance of the $C2/m$ superstructure reflections, the narrowing of the Li_2MnO_3-like ^{7}Li NMR resonances as well as the reappearance of the plateau in the first post-thermal charge. Furthermore, a loss of electrode mass was determined most probably including oxygen release from the cathode. In the subsequent five post-thermal cycles, the spinel-associated redox peaks S_{Mn} and S_{Ni} are clearly apparent in the dQ/dV plot, whereas an increase of the refined spinel phase content could not be identified directly after heating as well as after the five post-thermal cycles. Overall, these observations suggest a trend toward a spinel-type transition-metal cation ordering after the 300 cycles. During heating, the "metastable" structure probably segregates into a Li-rich pristine-like and a spinel phase along with the release of oxygen (densification) and accompanied by a reduction of the lattice strain. This post-thermal spinel phase is fully featured, including a clear allocation of the high-voltage redox peak S_{Ni} and the low-voltage peak S_{Mn}.

5. CONCLUSIONS

The findings of this work clearly emphasize the structural processes involved in the formation cycle as well as the subsequent electrochemical degradation in the investigated Li- and Mn-rich NCM cathode material with increasing number of cycles including the disappearance of the 4.5 V plateau and a pronounced voltage fade. It could be shown that the initially well-ordered layered structure and in particular the (Li/TM)-TM_6 honeycomb ordering within the transition-metal layers disappear on a long-range as well as on a very local atomic scale during the first charge and are replaced by a highly defective metastable state. The newly formed highly defective material exhibits a modified electronic structure and in particular an additional low-voltage redox process O_{def} in comparison to non-Li-rich and non-Mn-rich NCM cathodes. It could be shown that this redox process can be ascribed to the disappearance of the honeycomb ordering within the TM layers. The thermal treatment of discharged cathode samples, directly after formation or even after extensive cycling, induced a partial recovery of the pristine well-ordered state. This observation gives hope for recycling of these materials given that some features of the pristine material are recovered in electrochemistry including a reversal of the voltage fade. Furthermore, it could be shown that structural as well as electrochemical degradation can be induced either by electrochemical cycling or by thermal treatment of charged samples. Consequently, the thermodynamically more stable state can alternatively be formed by thermal treatment and may serve as an accelerated aging test for Li ion cathodes given that the electrochemistry after this 1 h test shows remarkable similarity to that obtained after 300 cycles. These findings could be very helpful for studying the mechanisms involved in the structural rearrangement during cycling as well as for identifying more stable compositions, coatings, or dopings for the commercial application of the Li- and Mn-rich materials.

■ ASSOCIATED CONTENT

Supporting Information

The Supporting Information is available free of charge at https://pubs.acs.org/doi/10.1021/acs.chemmater.9b04355.

TGA analysis; semiquantification of the oxygen release during heating; structural model used for Rietveld refinement; detailed presentation of the results; EC/NMR/XRD results of samples heated at 150, 200, and 250 °C; scanning electron microscopy (SEM)/EDX analysis of lithium anodes cycled against thermally treated cathodes; additional TM K edge XAS spectra; EXAFS-radial distribution function (RDF) analysis; soft-XAS O K edge spectra of thermally treated cathodes (PDF)

■ AUTHOR INFORMATION

Corresponding Author

Sylvio Indris − *Institute for Applied Materials—Energy Storage Systems (IAM-ESS), Karlsruhe Institute of Technology (KIT), Eggenstein-Leopoldshafen 76344, Germany;* orcid.org/0000-0002-5100-113X; Email: sylvio.indris@kit.edu

Authors

Florian Sigel − *Institute for Applied Materials—Energy Storage Systems (IAM-ESS), Karlsruhe Institute of Technology (KIT), Eggenstein-Leopoldshafen 76344, Germany; Department of Geo- and Material Science, Technische Universität Darmstadt, Darmstadt 64287, Germany;* orcid.org/0000-0002-0722-0626

Björn Schwarz − *Institute for Applied Materials—Energy Storage Systems (IAM-ESS), Karlsruhe Institute of Technology (KIT), Eggenstein-Leopoldshafen 76344, Germany*

Karin Kleiner − *Diamond Light Source, Oxfordshire OX11 0DE, United Kingdom*

Christoph Dräger − *Institute for Applied Materials—Energy Storage Systems (IAM-ESS), Karlsruhe Institute of Technology (KIT), Eggenstein-Leopoldshafen 76344, Germany;* orcid.org/0000-0002-9813-4378

Lars Esmezjan − *Institute for Applied Materials—Energy Storage Systems (IAM-ESS), Karlsruhe Institute of Technology (KIT), Eggenstein-Leopoldshafen 76344, Germany*

Murat Yavuz − *Institute for Applied Materials—Energy Storage Systems (IAM-ESS), Karlsruhe Institute of Technology (KIT), Eggenstein-Leopoldshafen 76344, Germany*

Helmut Ehrenberg − *Institute for Applied Materials—Energy Storage Systems (IAM-ESS), Karlsruhe Institute of Technology (KIT), Eggenstein-Leopoldshafen 76344, Germany; Department of Geo- and Material Science, Technische Universität Darmstadt, Darmstadt 64287, Germany;* orcid.org/0000-0002-5134-7130

Complete contact information is available at: https://pubs.acs.org/10.1021/acs.chemmater.9b04355

Notes

The authors declare no competing financial interest.

■ ACKNOWLEDGMENTS

Financial support from the Deutsche Forschungsgemeinschaft DFG within the Research Collaborative Centre 595 "Electrical Fatigue in Functional Materials" (Project T3) is gratefully acknowledged. This work has benefitted from beamtime allocation by the High Resolution Powder Diffraction Beamline P02.1 and the Applied X-ray Absorption Spectroscopy Beamline P65 at PETRA III at DESY, the Materials Science and Powder Diffraction Beam Line (MSPD) at ALBA as well as the Soft X-ray Spectroscopy and Microscopy Beamline WERA at KARA.

■ REFERENCES

(1) Thackeray, M. M.; Kang, S.-H.; Johnson, C. S.; Vaughey, J. T.; Benedek, R.; Hackney, S. A. Li2MnO3-Stabilized LiMO2 (M = Mn, Ni, Co) Electrodes for Lithium-Ion Batteries. *J. Mater. Chem.* **2007**, *17*, 3112.

(2) Assat, G.; Tarascon, J. Fundamental Understanding and Practical Challenges of Anionic Redox Activity in Li-Ion Batteries. *Nat. Energy* **2018**, *3*, 373.

(3) Croy, J. R.; Balasubramanian, M.; Gallagher, K. G.; Burrell, A. K. Review of the U.S. Department of Energy's "Deep Dive" Effort to Understand Voltage Fade in Li- and Mn-Rich Cathodes. *Acc. Chem. Res.* **2015**, *48*, 2813−2821.

(4) Dogan, F.; Croy, J. R.; Balasubramanian, M.; Slater, M. D.; Iddir, H.; Johnson, C. S.; Vaughey, J. T.; Key, B. Solid State NMR Studies of Li2MnO3 and Li-Rich Cathode Materials: Proton Insertion, Local Structure, and Voltage Fade. *J. Electrochem. Soc.* **2015**, *162*, A235−A243.

(5) Luo, K.; Roberts, M. R.; Hao, R.; Guerrini, N.; Pickup, D. M.; Liu, Y.-S.; Edström, K.; Guo, J.; Chadwick, A. V.; Duda, L. C.; et al. Charge-Compensation in 3d-Transition-Metal-Oxide Intercalation Cathodes through the Generation of Localized Electron Holes on Oxygen. *Nat. Chem.* **2016**, *8*, 684−691.

(6) Strehle, B.; Kleiner, K.; Jung, R.; Chesneau, F.; Mendez, M.; Gasteiger, H. A.; Piana, M. The Role of Oxygen Release from Li- and Mn-Rich Layered Oxides during the First Cycles Investigated by On-Line Electrochemical Mass Spectrometry. *J. Electrochem. Soc.* **2017**, *164*, A400−A406.

(7) Koga, H.; Croguennec, L.; Ménétrier, M.; Mannessiez, P.; Weill, F.; Delmas, C. Different Oxygen Redox Participation for Bulk and Surface: A Possible Global Explanation for the Cycling Mechanism of Li1.2Mn0.54Co0.13Ni0.13O2. *J. Power Sources* **2013**, *236*, 250−258.

(8) Assat, G.; Foix, D.; Delacourt, C.; Iadecola, A.; Dedryvère, R.; Tarascon, J. M. Fundamental Interplay between Anionic/Cationic Redox Governing the Kinetics and Thermodynamics of Lithium-Rich Cathodes. *Nat. Commun.* **2017**, *8*, No. 2219.

(9) Sathiya, M.; Rousse, G.; Ramesha, K.; Laisa, C. P.; Vezin, H.; Sougrati, M. T.; Doublet, M.-L.; Foix, D.; Gonbeau, D.; Walker, W.; et al. Reversible Anionic Redox Chemistry in High-Capacity Layered-Oxide Electrodes. *Nat. Mater.* **2013**, *12*, 827−835.

(10) Sathiya, M.; Abakumov, A. M.; Foix, D.; Rousse, G.; Ramesha, K.; Saubanère, M.; Doublet, M. L.; Vezin, H.; Laisa, C. P.; Prakash, A. S.; et al. Origin of Voltage Decay in High-Capacity Layered Oxide Electrodes. *Nat. Mater.* **2015**, *14*, 230−238.

(11) Croy, J. R.; Gallagher, K. G.; Balasubramanian, M.; Chen, Z.; Ren, Y.; Kim, D.; Kang, S.-H.; Dees, D. W.; Thackeray, M. M. Examining Hysteresis in Composite x Li2MnO3 ·(1−x)LiMO2 Cathode Structures. *J. Phys. Chem. C* **2013**, *117*, 6525−6536.

(12) Mohanty, D.; Li, J.; Abraham, D. P.; Huq, A.; Payzant, E. A.; Wood, D. L.; Daniel, C. Unraveling the Voltage-Fade Mechanism in High-Energy-Density Lithium-Ion Batteries: Origin of the Tetrahedral Cations for Spinel Conversion. *Chem. Mater.* **2014**, *26*, 6272−6280.

(13) Dogan, F.; Long, B. R.; Croy, J. R.; Gallagher, K. G.; Iddir, H.; Russell, J. T.; Balasubramanian, M.; Key, B. Re-Entrant Lithium Local Environments and Defect Driven Electrochemistry of Li- and Mn-Rich Li-Ion Battery Cathodes. *J. Am. Chem. Soc.* **2015**, *137*, 2328−2335.

(14) Key, B.; Dogan, F.; Long, B. R.; Croy, J. R.; Balasubramanian, M.; Slater, M. D.; Iddir, H.; Benedek, R.; Bettge, M.; Johnson, C. S. et al. *Solid State NMR Studies of Li-Rich NMC Cathodes: Investigating Structure Change and Its Effect on Voltage Fade Phenomenon*, Proceedings of the DOE Hydrogen Program and Vehicle Technologies Program Annual Merit Review, Washington, DC, June 16−20, 2014; U.S. Department of Energy: Washington, DC, 2014; p ES187.

(15) Robertson, A. D.; Bruce, P. G. Mechanism of Electrochemical Activity in Li2MnO3. *Chem. Mater.* **2003**, *15*, 1984−1992.

(16) Riekehr, L.; Liu, J.; Schwarz, B.; Sigel, F.; Kerkamm, I.; Xia, Y.; Ehrenberg, H. Fatigue in 0.5Li2MnO3:0.5Li(Ni1/3Co1/3Mn1/3)O2 Positive Electrodes for Lithium Ion Batteries. *J. Power Sources* **2016**, *325*, 391−403.

(17) Ito, A.; Shoda, K.; Sato, Y.; Hatano, M.; Horie, H.; Ohsawa, Y. Direct Observation of the Partial Formation of a Framework Structure for Li-Rich Layered Cathode Material Li-[Ni0.17Li0.2Co0.07Mn0.56]O2 upon the First Charge and Discharge. *J. Power Sources* **2011**, *196*, 4785−4790.

(18) de Biasi, L.; Schwarz, B.; Brezesinski, T.; Hartmann, P.; Janek, J. Chemical, Structural, and Electronic Aspects of Formation and Degradation Behavior on Different Length Scales of Ni-Rich NCM and Li-Rich HE-NCM Cathode Materials in Li-Ion Batteries. *Adv. Mater.* **2019**, *31*, No. 1900985.

(19) Singer, A.; Zhang, M.; Hy, S.; Cela, D.; Fang, C.; Wynn, T. A.; Qiu, B.; Xia, Y.; Liu, Z.; Ulvestad, A.; et al. Nucleation of Dislocations and Their Dynamics in Layered Oxide Cathode Materials during Battery Charging. *Nat. Energy* **2018**, *3*, 641−647.

(20) Dippel, A. C.; Liermann, H. P.; Delitz, J. T.; Walter, P.; Schulte-Schrepping, H.; Seeck, O. H.; Franz, H. Beamline P02.1 at PETRA III for High-Resolution and High-Energy Powder Diffraction. *J. Synchrotron Radiat.* **2015**, *22*, 675−687.

(21) Hammersley, A. P.; Svensson, S. O.; Hanfland, M.; Fitch, A. N.; Hausermann, D. Two-Dimensional Detector Software: From Real Detector to Idealised Image or Two-Theta Scan. *High Press. Res.* **1996**, *14*, 235−248.

(22) Rodríguez-Carvajal, J. Recent Advances in Magnetic Structure Determination by Neutron Powder Diffraction. *Phys. B: Condens. Matter* **1993**, *192*, 55−69.

(23) Welter, E.; Chernikov, R.; Herrmann, M.; Nemausat, R. A Beamline for Bulk Sample X-Ray Absorption Spectroscopy at the High Brilliance Storage Ring PETRA III. In *AIP Conference Proceedings*;Gwo, S.; Huang, D.-J.; Wei, D.-H., Eds.; American Institute of Physics: Melville, NY, 2019; Vol *2054*, p 040002.

(24) Mohanty, D.; Sefat, A. S.; Li, J.; Meisner, R. A.; Rondinone, A. J.; Payzant, E. A.; Abraham, D. P.; Wood, D. L., III; Daniel, C. Correlating Cation Ordering and Voltage Fade in a Lithium−Manganese-Rich Lithium-Ion Battery Cathode Oxide: A Joint Magnetic Susceptibility and TEM Study. *Phys. Chem. Chem. Phys.* **2013**, *15*, 19496.

(25) Pol, V. G.; Li, Y.; Dogan, F.; Secor, E.; Thackeray, M. M.; Abraham, D. P. Pulsed Sonication for Alumina Coatings on High-

Capacity Oxides: Performance in Lithium-Ion Cells. *J. Power Sources* **2014**, *258*, 46−53.
(26) Hausbrand, R.; Cherkashinin, G.; Ehrenberg, H.; Gröting, M.; Albe, K.; Hess, C.; Jaegermann, W. Fundamental Degradation Mechanisms of Layered Oxide Li-Ion Battery Cathode Materials: Methodology, Insights and Novel Approaches. *Mater. Sci. Eng., B* **2015**, *192*, 3−25.
(27) Oishi, M.; Yamanaka, K.; Watanabe, I.; Shimoda, K.; Matsunaga, T.; Arai, H.; Ukyo, Y.; Uchimoto, Y.; Ogumi, Z.; Ohta, T. Direct Observation of Reversible Oxygen Anion Redox Reaction in Li-Rich Manganese Oxide, Li2MnO3, Studied by Soft X-Ray Absorption Spectroscopy. *J. Mater. Chem. A* **2016**, *4*, 9293−9302.
(28) Cabana, J.; Casas-Cabanas, M.; Omenya, F. O.; Chernova, N. A.; Zeng, D.; Whittingham, M. S.; Grey, C. P. Composition-Structure Relationships in the Li-Ion Battery Electrode Material LiNi0.5Mn1.5O4. *Chem. Mater.* **2012**, *24*, 2952−2964.
(29) Bréger, J.; Jiang, M.; Dupré, N.; Meng, Y. S.; Shao-Horn, Y.; Ceder, G.; Grey, C. P. High-Resolution X-Ray Diffraction, DIFFaX, NMR and First Principles Study of Disorder in the Li2MnO3-Li[Ni1/2Mn1/2]O2 Solid Solution. *J. Solid State Chem.* **2005**, *178*, 2575−2585.
(30) Riekehr, L.; Liu, J.; Schwarz, B.; Sigel, F.; Kerkamm, I.; Xia, Y.; Ehrenberg, H. Effect of Pristine Nanostructure on First Cycle Electrochemical Characteristics of Lithium-Rich Lithium−Nickel−Cobalt−Manganese-Oxide Cathode Ceramics for Lithium Ion Batteries. *J. Power Sources* **2016**, *306*, 135−147.
(31) Kleiner, K.; Strehle, B.; Baker, A. R.; Day, S. J.; Tang, C. C.; Buchberger, I.; Chesneau, F.; Gasteiger, H. A.; Piana, M. Origin of High Capacity and Poor Cycling Stability of Li-Rich Layered Oxides: A Long-Duration in Situ Synchrotron Powder Diffraction Study. *Chem. Mater.* **2018**, *30*, 3656−3667.
(32) Bak, S. M.; Nam, K. W.; Chang, W.; Yu, X.; Hu, E.; Hwang, S.; Stach, E. A.; Kim, K. B.; Chung, K. Y.; Yang, X. Q. Correlating Structural Changes and Gas Evolution during the Thermal Decomposition of Charged LixNi0.8Co0.15Al0.05O2 Cathode Materials. *Chem. Mater.* **2013**, *25*, 337−351.
(33) Yoon, W.-S.; Iannopollo, S.; Grey, C. P.; Carlier, D.; Gorman, J.; Reed, J.; Ceder, G. Local Structure and Cation Ordering in O3 Lithium Nickel Manganese Oxides with Stoichiometry Li[NixMn(2−x)/3Li(1−2×)/3]O2. *Electrochem. Solid-State Lett.* **2004**, *7*, A167.
(34) Grey, C. P.; Dupré, N. NMR Studies of Cathode Materials for Lithium-Ion Rechargeable Batteries. *Chem. Rev.* **2004**, *104*, 4493−4512.
(35) Zheng, J.; Xu, P.; Gu, M.; Xiao, J.; Browning, N. D.; Yan, P.; Wang, C.; Zhang, J.-G. Structural and Chemical Evolution of Li- and Mn-Rich Layered Cathode Material. *Chem. Mater.* **2015**, *27*, 1381−1390.
(36) Gummow, R. J.; de Kock, A.; Thackeray, M. M. Improved Capacity Retention in Rechargeable 4 V Lithium/Lithium-Manganese Oxide (Spinel) Cells. *Solid State Ionics* **1994**, *69*, 59−67.
(37) Jiang, M.; Key, B.; Meng, Y. S.; Grey, C. P. Electrochemical and Structural Study of the Layered, "Li-Excess" Lithium-Ion Battery Electrode Material Li[Li1/9Ni1/3Mn5/9]O2. *Chem. Mater.* **2009**, *21*, 2733−2745.
(38) Dräger, C.; Sigel, F.; Indris, S.; Mikhailova, D.; Pfaffmann, L.; Knapp, M.; Ehrenberg, H. Delithiation/Relithiation Process of LiCoMnO4 Spinel as 5 V Electrode Material. *J. Power Sources* **2017**, *371*, 55−64.
(39) Grey, C. P.; Lee, Y. J. Lithium MAS NMR Studies of Cathode Materials for Lithium-Ion Batteries. *Solid State Sci.* **2003**, *5*, 883−894.
(40) Shimoda, K.; Murakami, M.; Komatsu, H.; Arai, H.; Uchimoto, Y.; Ogumi, Z. Delithiation/Lithiation Behavior of LiNi0.5Mn1.5O4 Studied by In Situ and Ex Situ 6,7Li NMR Spectroscopy. *J. Phys. Chem. C* **2015**, *119*, 13472−13480.
(41) Lee, Y. J.; Grey, C. P. 6Li Magic-Angle Spinning (MAS) NMR Study of Electron Correlations, Magnetic Ordering, and Stability of Lithium Manganese(III) Oxides. *Chem. Mater.* **2000**, *12*, 3871−3878.
(42) Shimoda, K.; Oishi, M.; Matsunaga, T.; Murakami, M.; Yamanaka, K.; Arai, H.; Ukyo, Y.; Uchimoto, Y.; Ohta, T.; Matsubara, E.; et al. Direct Observation of Layered-to-Spinel Phase Transformation in Li2MnO3 and the Spinel Structure Stabilised after the Activation Process. *J. Mater. Chem. A* **2017**, *5*, 6695−6707.
(43) Yamamoto, T. Assignment of Pre-Edge Peaks in K-Edge x-Ray Absorption Spectra of 3d Transition Metal Compounds: Electric Dipole or Quadrupole? *X-Ray Spectrom.* **2008**, *37*, 572−584.
(44) Oishi, M.; Fujimoto, T.; Takanashi, Y.; Orikasa, Y.; Kawamura, A.; Ina, T.; Yamashige, H.; Takamatsu, D.; Sato, K.; Murayama, H.; et al. Charge Compensation Mechanisms in Li1.16Ni0.15Co0.19Mn0.5O2 Positive Electrode Material for Li-Ion Batteries Analyzed by a Combination of Hard and Soft X-Ray Absorption near Edge Structure. *J. Power Sources* **2013**, *222*, 45−51.
(45) Yu, X.; Lyu, Y.; Gu, L.; Wu, H.; Bak, S.-M.; Zhou, Y.; Amine, K.; Ehrlich, S. N.; Li, H.; Nam, K.-W.; et al. Understanding the Rate Capability of High-Energy-Density Li-Rich Layered Li1.2Ni0.15Co0.1Mn0.55O2 Cathode Materials. *Adv. Energy Mater.* **2014**, *4*, No. 1300950.
(46) Nam, K.-W.; Bak, S.-M.; Hu, E.; Yu, X.; Zhou, Y.; Wang, X.; Wu, L.; Zhu, Y.; Chung, K.-Y.; Yang, X.-Q. Combining In Situ Synchrotron X-Ray Diffraction and Absorption Techniques with Transmission Electron Microscopy to Study the Origin of Thermal Instability in Overcharged Cathode Materials for Lithium-Ion Batteries. *Adv. Funct. Mater.* **2013**, *23*, 1047−1063.
(47) Yu, H.; Kim, H.; Wang, Y.; He, P.; Asakura, D.; Nakamura, Y.; Zhou, H. High-Energy "composite" Layered Manganese-Rich Cathode Materials via Controlling Li2MnO2 Phase Activation for Lithium-Ion Batteries. *Phys. Chem. Chem. Phys.* **2012**, *14*, 6584−6595.
(48) Kim, J.-S.; Johnson, C. S.; Vaughey, J. T.; Thackeray, M. M.; Hackney, S. A.; Yoon, W.; Grey, C. P. Electrochemical and Structural Properties of XLi2M'O3·(1-x)LiMn0.5Ni0.5O2 Electrodes for Lithium Batteries (M' = Ti, Mn, Zr; $0 \leq x \leqslant 0.3$). *Chem. Mater.* **2004**, *16*, 1996−2006.
(49) Genevois, C.; Koga, H.; Croguennec, L.; Ménétrier, M.; Delmas, C.; Weill, F. Insight into the Atomic Structure of Cycled Lithium-Rich Layered Oxide Li1.2Mn0.54Co0.13Ni0.13O2 Using HAADF STEM and Electron Nanodiffraction. *J. Phys. Chem. C* **2015**, *119*, 75−83.
(50) Boulineau, A.; Simonin, L.; Colin, J. F.; Canévet, E.; Daniel, L.; Patoux, S. Evolutions of Li1.2Mn0.61Ni0.18Mg0.01O2 during the Initial Charge/Discharge Cycle Studied by Advanced Electron Microscopy. *Chem. Mater.* **2012**, *24*, 3558−3566.

https://dx.doi.org/10.1021/acs.chemmater.9b04355
Chem. Mater. 2020, 32, 1210−1223